

A GRID OF 3D STELLAR ATMOSPHERE MODELS OF SOLAR METALLICITY: I. GENERAL PROPERTIES, GRANULATION AND ATMOSPHERIC EXPANSION

REGNER TRAMPEDACH

JILA, University of Colorado and National Institute of Standards and Technology, 440 UCB, Boulder, CO 80309, USA

AND

MARTIN ASPLUND AND REMO COLLET^{1,2}

Research School of Astronomy and Astrophysics, Mt. Stromlo Observatory, Cotter Road, Weston ACT 2611, Australia

AND

ÅKE NORDLUND²

Astronomical Observatory/Niels Bohr Institute, Juliane Maries Vej 30, DK-2100 Copenhagen Ø, Denmark

AND

ROBERT F. STEIN

Department of Physics and Astronomy, Michigan State University East Lansing, MI 48824, USA

Draft version August 29, 2018

ABSTRACT

Present grids of stellar atmosphere models are the workhorses in interpreting stellar observations, and determining their fundamental parameters. These models rely on greatly simplified models of convection, however, lending less predictive power to such models of late type stars.

We present a grid of improved and more reliable stellar atmosphere models of late type stars, based on deep, 3D, convective, stellar atmosphere simulations. This grid is to be used in general for interpreting observations, and improve stellar and asteroseismic modeling.

We solve the Navier Stokes equations in 3D and concurrent with the radiative transfer equation, for a range of atmospheric parameters, covering most of stellar evolution with convection at the surface. We emphasize use of the best available atomic physics for quantitative predictions and comparisons with observations.

We present granulation size, convective expansion of the acoustic cavity, asymptotic adiabat, as function of atmospheric parameters. These and other results are also available in electronic form.

Keywords: Stars: atmospheres – stars: late-type – stars: interiors – stars: fundamental parameters – physical data and processes: convection

1. INTRODUCTION

We present a homogeneous grid of three dimensional (3D) convective stellar atmosphere models, with applications to a wide range of astronomical inquiries. Previews of the grid have previously been given by Trampedach (2007); Trampedach & Stein (2011) with recent asteroseismic applications by Mathur et al. (2011, 2012) and Bonaca et al. (2012). The simulations have been computed with the Stein & Nordlund (1998)-code, but with updated atomic physics as described in more detail in Sect. 2. The solar abundance determination by Asplund et al. (2005) was based on a solar simulation identical to ours in all respects, except for a slightly higher horizontal resolution.

The first systematic analysis of convection in stellar atmospheres, through 3D simulations, was performed in the series of papers by Nordlund & Dravins (1990); Dravins & Nordlund (1990). They were interested in the 3D structure of granulation and the effects on spectral lines. These simulations were computed with an anelastic precursor to the present, fully compressible Stein &

Nordlund (1998)-code.

Currently an independent grid, the CIFIST grid (Ludwig et al. 2009), is being assembled using the CO⁵BOLD code (Wedemeyer et al. 2004; Freytag et al. 2012) to compute 3D simulations of late-type stars, including sub-solar metallicities and M-type stars.

A new grid of 3D convection simulations using the Stagger-code is nearing completion (Collet et al. 2011; Magic et al. 2013), and will encompass both sub- and super-solar metallicities. We are truly entering the age of 3D convective atmosphere simulations, and in combination with recent and soon to be realized observational advances, we are sure to learn much about the inner workings of stars in the coming decades.

This paper is an attempt at publishing results of 3D convection simulations in a format similar to what astronomers have been using for the last half a century: a grid in the atmospheric parameters effective temperature, T_{eff} , surface gravity, g , and metallicity, $[\text{Fe}/\text{H}]$. This grid, however, is only for solar metallicity, $[\text{Fe}/\text{H}] = 0$.

A major motivation for this effort, has been the advent of asteroseismology and the significant leap in stellar observations provided by the MOST (Walker et al. 2003), COROT (Baglin et al. 2002) and Kepler (Borucki et al. 2010) missions, and even by the star tracker on the failed infra-red satellite, WIRE (e.g., Bruntt et al. 2005). These

¹ Astronomical Observatory/Niels Bohr Institute, Juliane Maries Vej 30, DK-2100 Copenhagen Ø, Denmark

² Centre for Star and Planet Formation, Natural History Museum of Denmark, University of Copenhagen, Øster Voldgade 5–7, 1350 Copenhagen, Denmark

observations, with their highly stable, precision photometry and long time-lines, can reveal a wealth of detail about *field stars* that could previously only be considered for the Sun and a handful of other stars. The sheer volume of Kepler observations also means that a large range of stellar conditions are well sampled and meaningful statistics can be developed. The much anticipated launch in 2013 of the Gaia mission (Perryman et al. 2001; Prusti 2012) will greatly improve our knowledge of stellar distances, including for most Kepler targets, providing strong and independent constraints on absolute luminosities and radii. These observational advances demand reciprocal advances on the modeling side, and the present grid of convection simulations is our contribution to such an advance.

The present work is an alternative to previously published grids of 1D stellar atmosphere models. Some of the 1D atmosphere grids that have found widespread use have been constructed by Gustafsson et al. (2008, MARCS), Castelli & Kurucz (2003, ATLAS9) and Hauschildt et al. (1999a,b, NextGen-grid of PHOENIX models). These models vary in atomic and molecular line databases, continuum opacities, equation of state, whether they employ plane-parallel or spherical geometry and to what extent non-LTE effects are included. In all these cases radiative transfer is the focus and it is solved in impressive detail and with high accuracy. For late type stars, they also all share the same shortcoming: The analytical formulation of convection in the form of the widely used mixing length theory pioneered by Böhm-Vitense (1958, MLT) or the more recent variant by Canuto & Mazzitelli (1991, 1992). In contrast, the present atmosphere grid is based on explicitly evolving the Navier-Stoke's equations, as detailed in Sect. 2, with the hydrodynamics being directly coupled with realistic radiative transfer (see Sect. 2.3).

The lay-out of our grid of 37 simulations, is described in Sect. 2.5, where the issues of interpolating in the grid, and methods for averaging of the simulations are also discussed. General properties of convection in the simulations are discussed in Sect. 3, and contrasted with the analytical MLT approach. Here we also touch on the effect of 3D convection on the frequencies of p-modes.

The surface manifestation of convection on the Sun, has been observed for more than two centuries (Herschel 1801), with the term *granules* coined by Dawes (1864). Granulation on other stars has been rather elusive, though, with a tentative observation on Betelgeuse (α Ori) by Lim et al. (1998). Our simulations reproduce the quiet Sun granulation, both with respect to size, contrast and general shapes, giving us confidence in our predictions for other stellar parameters, as presented in Sect. 4. Recently, the unprecedented time-line, stability and precision of the Kepler observations, has allowed direct observations of the effect of granulation on integrated star light from red giants (Mathur et al. 2011). These observations were analyzed and compared with the present grid of simulations, and the agreement is generally good, although unresolved issues remain. A more detailed analysis, also including main sequence (MS) stars, will be carried out in the near future.

We round off with conclusions in Sect. 5.

2. THE 3D CONVECTION SIMULATIONS

The simulations evolve the fully compressible Navier-Stoke's equations for mass, momentum and energy conservation

$$\begin{aligned} \frac{\partial \ln \varrho}{\partial t} &= -\vec{u} \cdot \nabla \ln \varrho - \nabla \cdot \vec{u} \\ \frac{\partial \vec{u}}{\partial t} &= -\vec{u} \cdot \nabla \vec{u} + \vec{g} - \frac{P_g}{\varrho} \nabla \ln P_g + \frac{1}{\varrho} \nabla \cdot \vec{\sigma} \\ \frac{\partial \varepsilon}{\partial t} &= -\vec{u} \cdot \nabla \varepsilon - \frac{P_g}{\varrho} \nabla \cdot \vec{u} + Q_{\text{rad}} + Q_{\text{visc}} \end{aligned} \quad (1)$$

where ϱ is the density, P_g the gas pressure, ε the internal energy per unit mass, \vec{u} the velocity field and \vec{g} is the gravity, assumed to be constant with depth. This version of the equations, differ from the normal version, by having been divided by ϱ to pre-condition the equations for the very large density gradients in stellar surface layers.

The Stein & Nordlund (1998)-code used here is a non-staggered, finite difference code. Derivatives and interpolations are evaluated from cubic splines and time is advanced with a third order leapfrog (predictor/corrector) scheme (Hyman 1979; Nordlund & Stein 1990).

As all higher-order (higher than linear) order schemes are unstable artificial diffusion is needed for stabilizing the solution. We employ a quenched hyper-diffusion scheme which efficiently concentrates the diffusion at sharp changes in variables, leaving the smoother parts of the solution unaffected. Hyper-diffusion means a fourth-order term is added to the normal second-order (Laplacian) term, and the quenching consists of ensuring the fourth-order term everywhere has the same sign as the second order term, to not excite more ringing. This is explained in more detail by Stein & Nordlund (1998). This does not constitute a sub-grid scale model, as we have not specified any preconceptions of what should happen below the grid-scale of our simulations. That in turn implies that those scales do not contribute any significant net fluxes, i.e., motions on that scale are considered isotropic turbulence.

This diffusion by the viscous stress tensor $\vec{\sigma}$, gives rise to the dissipation, $Q_{\text{visc}} = \sum_{ij} \sigma_{ij} \partial u_i / \partial r_j$, in Eq. (1). The radiative heating, Q_{rad} , is dealt with in more detail in Sect. 2.3.

Each of the simulations has been performed on a $150 \times 150 \times 82$ rectangular grid with equidistant and cyclic horizontal grid and a vertical (smooth) grid which is optimized to capture the large temperature gradients in the photosphere. The simulations cover about 13 pressure scale-heights vertically, with half of those below and half above the photosphere. On a Rosseland optical depth scale, this corresponds to $\log_{10} \tau_{\text{Ross}} = [-4.5; 5-8]$. This is the region we will refer to as *stellar surface layers*. The effects of numerical resolution on stratification and velocity fields have been explored by Asplund et al. (2000a), on which we based our choice of resolution.

Both the top and bottom boundaries are penetrable with outflows leaving undisturbed. To approximate the effect of the convection zone below the simulation domain, *inflows* at the bottom boundary are evolved towards a constant entropy, hydrostatic equilibrium and a vertical velocity that balances the mass flux of the unaltered outflows. The inflows are evolved towards this ideal solution, on time-scales of half the minimum flow-crossing time at the bottom, which means the inflow pro-

files are not entirely flat. The entropy is in practice set by values of density and internal energy. The total flux of the simulation, σT_{eff}^4 , is solely due to the supplied entropy of the inflows—no artificial fluxes are imposed anywhere. Effects of the bottom boundary are imperceptible in temperature, pressure and density, but recognized in entropy, superadiabatic gradient and velocities, for which they affect the bottom 5–10 grid-points, covering 0.6–1.0 pressure scale-heights. The top boundary is a fiducial layer, located three times further away from the first grid point in, than the next. This together with the exponentially declining density, ensures only little mass is present there, and minimizes its influence on the simulation. Velocities and energies from the first grid point are simply copied to the fiducial layer, and the density is extrapolated hydrostatically.

2.1. Atomic Physics

We employ the so-called Mihalas-Hummer-Däppen (MHD) equation of state (EOS) (Hummer & Mihalas 1988; Mihalas et al. 1988; Däppen et al. 1988) which includes explicit dissociation, ionization and excitation of all states of all species of all included elements. The only two molecular species included are H_2 and H_2^+ , however. We have custom calculated tables of this EOS for the chemical mixture listed in Table 1, which includes 15 elements as opposed to the previously published 6 element mixtures. As the dependent variables of the Navier-Stokes equations are ϱ and ε , we invert the EOS table to one in $(\ln \varrho, \varepsilon)$. The entropy is evaluated by integration of the table

$$S = S_0 + \int \frac{1}{T} \left(d\varepsilon - \frac{p_{\text{gas}}}{\varrho} d \ln \varrho \right), \quad (2)$$

where we first integrate along iso-chores of the table and then along the internal energy axis. The integration constant, S_0 , is (arbitrarily) chosen so as to have zero-point at $\varrho = \sqrt{10} \times 10^{-7} \text{ g cm}^{-3}$ and $\varepsilon = 2.5 \times 10^{12} \text{ erg cm}^{-3}$.

The bound-free and free-free opacities, as well as scattering cross-sections are calculated using the MARCS package of codes (Gustafsson 1973), which is the engine behind the MARCS stellar atmosphere models (Gustafsson et al. 1975, 2008). The data-tables, however, are updated as follows:

We have included the absorption by H^- bound-free (bf) (Broad & Reinhardt 1976; Wishart 1979), free-free (ff) (Bell & Berrington 1987), H_2^+ bf+ff (Stancil 1994), H_2^- ff (Bell 1980), and the photo-dissociation of OH and CH (Kurucz et al. 1987). The most important levels of He I, C I, N I, O I, Na I, Mg I, Mg II, Al I, Si I, Ca I, Ca II and Fe I were included as simple analytical fits as listed by Mathisen (1984). Bound-free absorption by O I and C II were adopted from the MARCS (Gustafsson et al. 2008) implementation of OP opacities (Butler & Zeppen 1990; Yan & Seaton 1987). Most of these changes were described in more detail by Trampedach (1997).

Rayleigh scattering is included as fits to the results by Gavrila (1967) for H I, Langhoff et al. (1974) for He I and by Victor & Dalgarno (1969) for H_2 . The usual Thomson scattering by free electrons is also included.

The line opacity is supplied by the opacity distribution functions (ODFs) of Kurucz (1992a,b), which include 58 million lines from the first nine ions of all ele-

Table 1
Logarithmic abundances normalized to $A(\text{H}) = 12$.

Z	Elem.	Abund.	Z	Elem.	Abund.
1	H	12.00	14	Si	7.51
2	He	10.92	16	S	7.17
6	C	8.52	18	Ar	6.52
7	N	8.01	19	K	5.08
8	O	8.89	20	Ca	6.32
10	Ne	8.05	24	Cr	5.63
11	Na	6.29	26	Fe	7.50
12	Mg	7.54	28	Ni	6.21
13	Al	6.43			

ments through Ni and the diatomic molecules H_2 , CO, CH, CN, C_2 , NH, OH, MgH, SiH, SiO and TiO.

2.2. Chemical Abundances

The Solar abundances we use, are listed in Table 1 as logarithmic abundances normalized to $A(\text{H}) = 12.00$. In our adaptation of atomic physics, the abundances enter in three independent places; In the EOS calculation, the bf- and ff-opacities and in the line opacities supplied by the ODFs. Since we have calculated our own tables of the MHD EOS and perform our own calculation of bf- and ff-opacities using the MARCS package, we are free to choose the abundances for those two parts – only restricted in the choice of elements by the availability of the necessary atomic physics.

For the ODFs, however, we have less control over the assumed composition, and we have therefore largely adopted the abundances prescribed by the available ODFs at the time of starting the simulation grid. Kurucz (1992a,b) has made ODF tables available for the abundances by Anders & Grevesse (1989, AG89 hereafter) for a range of metallicities, but also for a He-free mixture and a few tables for lower Fe abundances. This enabled us to perform interpolations to the helioseismically determined Solar He abundance of $A(\text{He}) = 10.92$ (down from the classic value of $A(\text{He}) = 11.00$) Basu & Antia (1995); Basu (1998) and the more modern Fe abundance of 7.50 (Grevesse & Sauval 1998; Asplund et al. 2009) (down from 7.67). These interpolations resulted in the abundances listed in Table 1. The differences between ours and the recent abundances based on solar convection simulations, (Asplund et al. 2009, AGSS'09), are rather small and not systematic, except for the decreased C, N and O abundances. These three elements, however, have little effect on atmospheric structure, as they supply only little line or continuum opacity, and affect the EOS minimally compared to the ionization of hydrogen (they have ionization energies similar to H). The only significant influence is through the molecules of H, C, N and O. Solar ATLAS9 models by Castelli & Kurucz (2003, only on-line) show very small differences in structure, though, between GS'98 and AGS'05: The latter is 20 K warmer at $\log \tau_{\text{Ross}} = -6.0$ decreasing linearly to a few Kelvins around the photosphere and is about 30 K cooler below $\log \tau_{\text{Ross}} \sim 1$. AGSS'09 has C, N and O abundances that are closer to the "classic" GS'98 values, than does AGS'05, and we expect the above differences to be even smaller.

For these reasons we did not feel compelled to recompute the, at that time, mostly finished grid of simulations to adopt the new abundances.

2.3. Radiative Transfer

The radiative transfer in the atmosphere, has been described in detail by Nordlund (1982); Nordlund & Dravins (1990); Stein & Nordlund (2003). The forward solution is performed on long characteristics, and the original Feautrier (1964)-technique (See also Mihalas 1978), has been modified to give more accurate solutions in the optical deep layers Nordlund (1982). The angle to the vertical of an outgoing characteristic (or ray) is $\mu = \cos \theta$ and the azimuthal angle is φ .

The angular integrations are performed with $N_\varphi = 4$ φ -angles and $N_\mu = 2$ μ -angles with μ -points and -weights determined by Radau quadrature (Radau 1880; Abramowitz & Stegun 1964). This method ensures the highest accuracy when one end-point (the vertical) is to be included. For $N_\mu = 2$ this method gives $\theta = 0^\circ$ and 70° with weights $\frac{1}{4}$ and $\frac{3}{4}$. The ϕ -angles are rotated for each time-step to avoid developing preferred directions. To perform radiative transfer on slanted rays, the whole simulation cubes are rotated and tilted by rotating and shifting each horizontal plane sideways, exploiting the periodic boundaries. This is performed with bi-cubic spline interpolation. The number of grid-points in the inclined cubes is the same as in the normal, vertical cube, and the computational cost is therefore also the same for the vertical as for each (μ, ϕ) inclined calculation of the radiative transfer.

The effects of spectral lines are included through the method of opacity binning. This consists of grouping wavelengths together based on their opacity strength, or more precisely, the Rosseland optical depth, τ_{Ross} , at which the monochromatic optical depth is $\tau_\lambda = 1$. We use four bins, with each bin spanning a decade in opacity strength. The source function used for each bin is simply the Planck function, $B_\lambda(T)$, summed up over the wavelengths, λ_j , in each bin, i ,

$$B_i w_i = \sum_{j(i)} B_{\lambda_j} w_{\lambda_j}, \quad w_i = \sum_{j(i)} w_{\lambda_j}. \quad (3)$$

The weights, w_{λ_j} , for each wavelength is simply the wavelength width of each ODF, multiplied by the weight of each bin in the ODF. This method of opacity binning ensures that the radiative cooling and heating in the photosphere of strong lines is included as well as that of the continuum. The radiative heating per volume is

$$Q_{\text{rad}} = 4\pi \varrho \int_\lambda \kappa_\lambda (J_\lambda - S_\lambda) d\lambda \quad (4)$$

$$\simeq 4\pi \varrho \kappa_{\text{Ross}} \sum_i x_i (J_i - B_i) w_i, \quad (5)$$

where J_λ is the zero'th angular moment of the specific intensity, λ . The general source function, S_λ , has been replaced by the strict LTE counterpart, B_λ . This means scattering has *not* been included (see Skartlien 2000; Hayek et al. 2010, for effects of scattering and a consistent formulation of it), except as absorption in the Rosseland mean (see below). The wavelength integration of Eq. (4) is approximated by the summing over bins, i , reducing the problem by about four orders of magnitude compared to a monochromatic calculation. The relative opacity, $x_i = \kappa_i / \kappa_{\text{Ross}}$, defines the bin-wise optical depth $\tau_i = \int \varrho \kappa_{\text{Ross}} x_i dz$. For each bin, J_i and B_i will diverge

for $\tau_i \lesssim 1$, giving rise to first cooling in the photosphere, and then heating higher up in the atmosphere as B_i follows the temperature and J_i converges to a constant. The fraction of heating/cooling contribution from each bin depends largely on the fraction of the source function, $B_i(\tau_i \sim 1)w_i$, contained in that bin.

The bin membership of each wavelength is determined from a 1D, monochromatic radiative transfer calculation, performed on the average stratification of the simulation, averaged over a whole number of p modes (to yield a stable average). The bin membership is found as the Rosseland optical depth at which the given wavelength has unity optical depth

$$i = \text{int}[\log_{10} \tau_{\text{Ross}}(\tau_\lambda = 1)], \quad i \in \{0, 1, 2, 3\}, \quad (6)$$

where 'int' denotes the nearest integer. Wavelengths that go outside this range are assigned to the continuum bin, $i = 0$, or the strong-lines bin, $i = 3$, respectively. For expediency we choose to simply scale the opacity of the continuum bin, such that $\kappa_i = 10^i \kappa_0$. The proper opacity average within each bin, will need to converge to the diffusion approximation at depth, and the free-streaming approximation in the high atmosphere. We therefore choose a bridging

$$\kappa_0 = e^{-2\tau_{\text{Ross},0}} \kappa_J + (1 - e^{-2\tau_{\text{Ross},0}}) \kappa_{\text{Ross},0}, \quad (7)$$

between the Rosseland mean of the continuum bin and mean-intensity weighted opacity. These are defined as

$$\kappa_{\text{Ross},0}^{-1} = \sum_{j(i=0)} \frac{1}{\kappa_{\lambda_j} + \sigma_{\lambda_j}} \frac{\partial B_{\lambda_j}}{\partial T} w_{\lambda_j} \bigg/ \sum_{j(i=0)} \frac{\partial B_{\lambda_j}}{\partial T} w_{\lambda_j}, \quad (8)$$

where $j(i = 0)$ is the set of wavelengths forming the continuum bin, according to Eq. (6). This Rosseland mean includes both the monochromatic absorption, κ_λ , and monochromatic scattering, σ_λ , coefficients.

The mean-intensity weighted opacity, κ_J , is summed over all wavelengths, but altered to suppress optically deep wavelengths with a factor $e^{-\tau_{\lambda_j}/2}$

$$\kappa_J = \sum_j \kappa_{\lambda_j} J_{\lambda_j} e^{-\tau_{\lambda_j}/2} w_{\lambda_j} \bigg/ \sum_j J_{\lambda_j} e^{-\tau_{\lambda_j}/2} w_{\lambda_j}. \quad (9)$$

Note how scattering is *not* included in κ_J , except through the optical depth, $d\tau_\lambda = \varrho(\kappa_\lambda + \sigma_\lambda)dz$, in the suppression factor. The mean-intensity weighted opacity, κ_J , depends directly on the 1D radiative transfer solution for the mean intensity, J_λ . To cover the whole opacity table, we extrapolate $\kappa_J / \kappa_{\text{Ross},0}^{-1}$ from the 1D calibration stratification to the rest of the table. This is done along fits in $\log T$ and $\log \varrho$ to iso-optical depth contours of the simulation. These tables are therefore specific to each individual simulation.

In plane-parallel, gray radiative transfer calculations, the atmosphere converges to an iso-therm with height (King 1956, $0.81119 \times T_{\text{eff}}$), as there is no heating or cooling above $\tau \sim 0.1$. In a line blanketed atmosphere, on the other hand, there are separate cooling peaks from lines of a range of strengths as outlined above, resulting in atmospheres with decreasing temperatures with height and various features arising from the underlying opacities.

In deep layers, with continuum optical depth $\tau_1 > 300$ for all points in the plane, we have added the radiative flux and its associated heating, as calculated in the diffusion approximation.

2.3.1. Radiative contributions to the EOS

The EOS tables already include the radiative contributions in the diffusion approximation, in particular for energy, $\varepsilon_{\text{rad}}^{\text{deep}} = aT^4/\rho$, and pressure, $p_{\text{rad}}^{\text{deep}} = \frac{a}{3}T^4$. The radiation density constant is $a = 8\pi^5 k^4 / (15c^3 h^3)$. We use the 1D, monochromatic calibration to evaluate the proper expressions in the atmosphere

$$\varepsilon_{\text{rad}} = \frac{4\pi J}{c} \frac{J}{\rho} = \varepsilon_{\text{rad}}^{\text{deep}} \frac{J}{B}, \quad (10)$$

and

$$p_{\text{rad}} = \frac{4\pi K}{c} K = p_{\text{rad}}^{\text{deep}} \frac{K}{B}. \quad (11)$$

where K is the second angular moment of the specific intensity. We therefore add $p_{\text{rad}}^{\text{deep}}(\frac{K}{B} - 1)$ to the pressure of the EOS table and equivalently to the internal energy. The J/B - and K/B -ratios are extrapolated from the 1D average to the rest of the table, as described above.

2.4. Relaxing the Simulations

A simulation for a new choice of $(T_{\text{eff}}, \log g)$ -parameters is started from a previous simulation with similar parameters. The physical dimensions of the simulation box is scaled by the ratio of gravitational accelerations and the average entropy structure is changed to result in a new T_{eff} based on all the previous simulations of the grid. The behavior of the entropy in the asymptotically deep interior, with atmospheric parameters, is shown in Fig. 1. This asymptotic entropy is also what we feed into the simulations through the upflows at the bottom boundary, as confirmed from exponential fits to the horizontally averaged upflow entropy. The boundary affects the entropy by prematurely pulling it up to the asymptotic value, over the bottom 4–5 grid-points (0.3–0.5 pressure scale-heights). This boundary effect on entropy is small, though—only 0.4–1.5% of the atmospheric entropy jump.

If we adjust only $\log g$ (with the associated scaling of the size of the box), but keep the entropy unchanged, the new simulation will end up along the adiabat of the original simulation and at the new $\log g$. From Fig. 1 we see that those adiabats are diagonals in the plot. Many of the simulations lie along such adiabats, as this is the simplest and fastest way of starting a new simulation. The scaling of the box, should conceivably be accompanied by some scaling of the velocities. It turns out, however, that a factor of 10^2 change in g results in only a factor of 1.5 change in vertical velocities (1.3 for horizontal velocities). Keeping the fluxes consistent through the change, by not changing the velocities, seemed a better approach. These simulations will slump or expand, necessitating a new optimization of the vertical scale and extent.

If T_{eff} needs to be adjusted away from the starting simulations adiabat, more complicated adjustments must be invoked. First we shift the average entropy to the new S_{max} and linearly stretch the average entropy stratification from the bottom to the atmospheric entropy minimum, to match the entropy jump. The expected jump

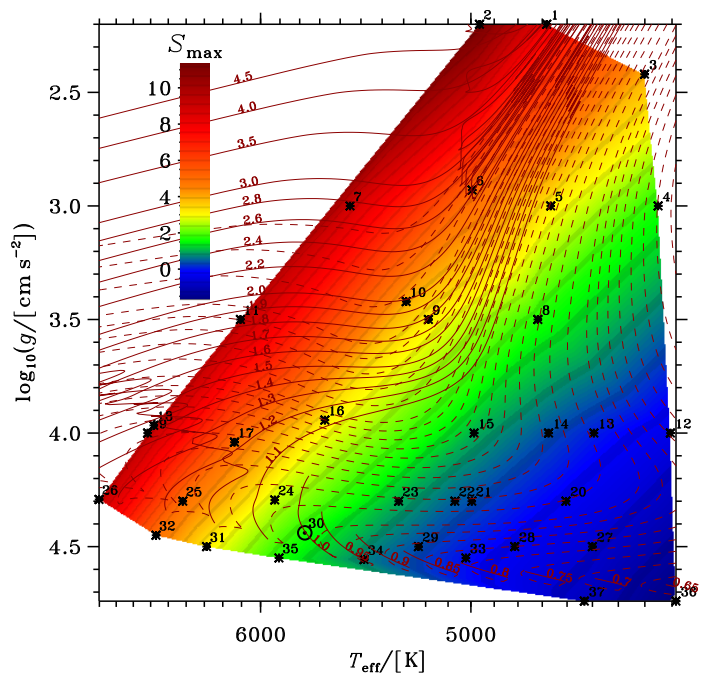


Figure 1. The asymptotic entropy (arbitrary zero-point, see below Eq. [2]), $S_{\text{max}}/[10^8 \text{ erg g}^{-1} \text{ K}^{-1}]$, of the deep convection zone as function of stellar atmospheric parameters. The T_{eff} -scale is logarithmic. The entropy is indicated with colors as shown on the color bar, and the location of the simulations are shown with black asterisks, except for the solar simulation which is indicated with a \odot . For this figure only, we also added the simulation number from table 2. We have over-plotted tracks of stellar evolution computed with the MESA-code (Paxton et al. 2011), for masses as indicated along each track. The dashed part shows the pre-main-sequence contraction, and α and initial helium abundance, Y_0 , were determined from a calibration to the present Sun.

and S_{max} are found from inter-/extra-polations in Figs. 1 and 4 between the previous simulations. We assume the simulations to be homologous on a gas pressure scale, $p_{\text{sc}} = p_{\text{gas}}/p_{\text{gas}}(\text{peak in } p_{\text{turb}})$, normalized at the location of the maximal $p_{\text{turb}}/p_{\text{tot}}$ -ratio. The whole simulation cube is therefore adjusted adiabatically by the same pressure factor, and then adjusted iso-barically to the new entropy stratification. Our method does not rely on linearity of the EOS, but solves numerically for entropy along pressure contours. In both cases the changes, $\Delta \ln \rho$ and $\Delta \varepsilon$, are found from the average stratification only, but applied to the whole cube.

With these new pressures and densities, we scale the vertical velocities, u_z , to result in the projected peak $p_{\text{turb}}/p_{\text{tot}}$ -ratio. We then adjust the amplitude of the internal energy fluctuations (keeping all the carefully adjusted averages unchanged) in order to reproduce the target convective flux. We find a hydrostatic z -scale by inverting the equation of hydrostatic equilibrium

$$\frac{dP}{dz} = g\rho \quad \Leftrightarrow \quad z = \int_{P_{\text{tot, bot}}}^{P_{\text{tot}}(z)} \frac{dP_{\text{tot}}}{g\rho}, \quad (12)$$

and integrating from the bottom and up. This z -scale will be rugged and not optimal for resolving the hydro- and thermo-dynamics. The last step is therefore to compute an optimized z -scale and interpolate the simulation cubes to this. This procedure results in simulations that are rather close to their (quasi-static) equilibrium state,

minimizing the relaxation time.

No matter how carefully such a scaled simulation has been constructed, it will still not be in its new (quasi-static) equilibrium configuration, since we do not know *a priori* what that equilibrium is—that is the whole reason we need to perform these simulations, after all. The natural state is the lowest energy state, so departure from equilibrium means an excess of energy. This extra energy is quickly spent on exciting p modes (sound waves) and over a few sound crossing times, the energy gets channeled into 3–4 of the lowest order modes of the simulation box (radial, as well as non-radial). We extract surplus energy from the simulation by damping the radial p modes by adding a term

$$-\frac{v_{\text{mode}}}{t_{\text{damp}}}, \text{ with } v_{\text{mode}} = \frac{\langle \rho u_z \rangle}{\langle \rho \rangle}, \quad (13)$$

to the radial part of the momentum equation, Eq. (1b). For the damping time-scale, t_{damp} , we use 1.3 times the period of the fundamental p mode, P_1 . When the center-of-mass velocity of the simulation no longer displays simple sinusoidal modes, the damping time is increased smoothly (exponentially) until the damping is insignificant at which point it is turned off. The simulation is run without damping for another $2P_1$ for which we compute horizontal averages of ρ and T . This constitutes the first iteration of the relaxation process.

If the stratification has changed from the previous iteration, the opacity binning is re-calculated with the new stratification and we start a new iteration of the relaxation process (from Eq. (13)). Otherwise we can start the production runs, from which the results in this paper are based. Each production run covers at least $10P_1$ and all snapshots (about 100–300) of each simulation are included in the averaging producing our results.

Some further requirements for a relaxed simulation are that the fluxes have reached a statistically steady state, that the total flux is statistically constant, that no quantities (especially at the bottom boundary) show any significant drift, that the radiative heating is statistically constant and that the time-steps are like-wise. All these precautions ensure that we have a homogeneous set of simulations and that we can trust in the differences between the simulations and therefore can trust the dependencies of derived quantities with T_{eff} and $\log g$.

2.5. The Grid of Simulations

Our 37 simulations span most of the convective range of the zero age main sequence (ZAMS) from $T_{\text{eff}} = 4\,300\text{ K}$ to $6\,900\text{ K}$ (K5–F3) and up to giants of $\log g = 2.2$ between $T_{\text{eff}} = 5\,000\text{ K}$ and $4\,200\text{ K}$ (K2–K5), as listed in table 2. The location of the simulations in the atmospheric HR-diagram is also shown in Fig. 1.

Our grid of simulations is not regular, for a couple of practical reasons. The most important one being that T_{eff} is not an actual parameter of the simulations. We only have indirect control over T_{eff} , by adjusting the entropy of the upflows entering through the bottom boundary. Requiring particular values of T_{eff} would add another outer loop of iterations of the relaxation process (Sect. 2.4), for monitoring and adjusting the resulting T_{eff} . Since this takes extra (human) time we have not required a regular grid and pre-determined values of T_{eff} .

This is the reason that many of the simulations lie along adiabats of the deep entropy, as shown in Fig. 1. Those simulations result from changes to $\log g$ (with the associated scaling of the size of the box) only, without adjusting the entropy structure. The entropy structure, of course, changes during the subsequent relaxation of the simulation, but the asymptotic deep value is fixed.

Not insisting on a regular grid, also has the advantage of being able to have higher resolution around the main sequence, where it is most needed. This makes it possible to resolve features that would be missed in a coarser, regular grid.

2.5.1. Interpolating in the Grid

Interpolation in such an irregular ($\log T, \log g$)-grid is a bit more complicated compared to other grids of stellar atmospheres. Fortunately the triangulation of arbitrarily distributed points in a plane is not a new discipline. We use the suite of Fortran77 routines developed by Renka (1984), which performs both the triangulation and subsequent interpolations by piece-wise cubic 2D functions. The routines can also return the partial derivatives of the interpolation. The triangulation routines supplied in IDL³ are also based on Renka (1984), facilitating visualization and interactive debugging.

It makes no sense to interpolate individual snapshot of whole simulation cubes between different simulations, since they will not be homologous. We therefore only interpolate between temporally and horizontally averaged structures, or between derived quantities, e.g., limb darkening coefficients or the intensity contrast of granulation.

2.5.2. Averaging Procedures

The averaging of the simulations is carried out in two ways. First, a horizontal averaging mapped onto a (horizontally averaged) column density scale in order to filter out the main effect of the radial p-modes excited in the simulations. We call this pseudo Lagrangian averaging and denote it by $\langle \dots \rangle_L$. The reason for the “pseudo” is the use of a 1D average column density scale, as opposed to the local column density.

The second method we employ, is an optical depth averaging performed by averaging the quantities in question, over the undulating iso- τ surfaces. This average we denote by $\langle \dots \rangle_\tau$ and it has been calculated for both the Rosseland optical depth, τ_{Ross} and the $5\,000\text{ \AA}$ monochromatic optical depth, τ_{5000} .

What kind of average, to use, depends on the problem at hand, and should be guided by the structure of the equations involved (before approximations and simplifications are made).

3. GENERAL PROPERTIES OF SURFACE CONVECTION

Deep convection is very nearly adiabatic (to parts per million), whether it occurs in the core of stars, or in the envelope. Here, no theory of convection is necessary for determining the structure of the star, as the stratification just follows an adiabat. This property makes deep convection very attractive for EOS research (Däppen & Gough 1984; Däppen & Nayfonov 2000), since the adia-

³ IDL[®] is a registered trademark of ITT Visual Information Solutions, USA.

Table 2
Fundamental parameters for the 37 simulations, and a few derived quantities.*

sim ^a	MK class ^b	T_{eff} [K]	$\log g$	w^c [Mm]	d^d [Mm]	Δz^e [Mm]	A_{gran}^f [Mm]	Λ^g [Mm]	S_{max}^h	S_{jump}^h	$\frac{P_{\text{turb}}}{P_{\text{tot}}}$	$\frac{I_{\text{RMS}}}{\langle I \rangle}$
1	K3	4681 ± 19	2.200	1248.30	652.410	3.478–16.695	283.010	78.495	7.9539	6.7934	0.26223	0.18555
2	K2	4962 ± 21	2.200	1800.00	958.370	4.598–27.616	382.270	170.020	11.3540	9.5480	0.29639	0.18758
3	K5	4301 ± 17	2.420	667.81	409.900	1.724–12.100	136.080	32.745	3.9781	3.2772	0.19130	0.17758
4	K6	4250 ± 11	3.000	165.00	78.271	0.457–1.815	31.953	3.805	1.6903	1.6152	0.14336	0.16793
5	K3	4665 ± 16	3.000	169.47	115.880	0.649–2.564	36.060	6.236	3.1968	2.7581	0.16881	0.17371
6	K1	4994 ± 15	2.930	275.67	132.840	0.591–3.752	50.140	9.476	5.1703	4.4027	0.20124	0.17806
7	G8	5552 ± 17	3.000	328.29	160.950	0.787–4.101	52.785	17.077	8.7944	7.5617	0.26233	0.19568
8	K3	4718 ± 15	3.500	52.18	30.682	0.176–0.751	11.005	1.203	1.7158	1.7188	0.13479	0.15879
9	K0	5187 ± 17	3.500	53.59	36.937	0.196–0.891	11.372	1.826	3.1948	2.8700	0.17238	0.17183
10	K0	5288 ± 20	3.421	89.00	38.936	0.205–0.958	15.609	2.391	3.9879	3.5133	0.17966	0.17845
11	F9	6105 ± 25	3.500	71.01	52.645	0.220–1.416	17.123	5.964	9.2519	8.0430	0.27125	0.20493
12	K6	4205 ± 8	4.000	14.83	6.342	0.039–0.138	2.753	0.116	-0.3701	0.5958	0.07684	0.11957
13	K4	4494 ± 9	4.000	14.83	6.420	0.046–0.113	2.981	0.165	0.1071	0.7660	0.09391	0.13550
14	K3	4674 ± 8	4.000	14.83	7.437	0.034–0.204	2.945	0.216	0.4342	0.9427	0.10296	0.13596
15	K2	4986 ± 13	4.000	16.50	9.026	0.058–0.196	3.273	0.299	1.0546	1.3418	0.11742	0.14480
16	G6	5674 ± 16	3.943	19.33	12.785	0.069–0.285	4.069	0.663	3.1889	2.9713	0.17173	0.19793
17	F9	6137 ± 14	4.040	21.40	9.326	0.041–0.300	4.019	0.747	4.9301	4.4363	0.20478	0.20117
18	F4	6582 ± 26	3.966	24.28	18.246	0.092–0.421	6.034	2.087	9.2444	8.1239	0.26844	0.21381
19	F4	6617 ± 33	4.000	22.45	16.877	0.085–0.389	5.368	1.936	9.2407	8.1188	0.25049	0.21202
20	K4	4604 ± 8	4.300	7.43	3.625	0.017–0.101	1.405	0.076	-0.2001	0.6473	0.08236	0.12048
21	K1	4996 ± 17	4.300	7.43	3.772	0.019–0.096	1.515	0.113	0.4301	0.9887	0.10066	0.13029
22	K1	5069 ± 11	4.300	8.27	3.531	0.023–0.074	1.615	0.115	0.5441	1.0562	0.10300	0.13118
23	K0	5323 ± 16	4.300	8.27	4.135	0.023–0.096	1.614	0.145	1.0413	1.3973	0.11662	0.14201
24	G1	5926 ± 18	4.295	9.32	5.473	0.024–0.139	1.872	0.259	2.6796	2.6358	0.15869	0.18234
25	F5	6418 ± 26	4.300	11.76	5.373	0.030–0.128	2.221	0.406	4.9238	4.4645	0.20351	0.20745
26	F2	6901 ± 29	4.292	11.45	8.334	0.037–0.232	2.760	0.978	9.2408	8.1679	0.27642	0.20984
27	K4	4500 ± 4	4.500	4.69	2.108	0.013–0.051	0.886	0.031	-0.6094	0.4978	0.06359	0.11046
28	K3	4813 ± 8	4.500	4.69	2.026	0.010–0.054	0.949	0.049	-0.2102	0.6576	0.07991	0.11609
29	K0	5232 ± 12	4.500	4.69	2.344	0.011–0.062	1.017	0.071	0.4277	1.0217	0.10218	0.12981
30	G5	5774 ± 17	4.438	6.02	3.476	0.020–0.082	1.237	0.140	1.7112	1.9149	0.13747	0.16345
31	F7	6287 ± 15	4.500	5.36	3.498	0.020–0.074	1.178	0.179	3.1827	3.0738	0.16893	0.19410
32	F4	6569 ± 17	4.450	8.33	3.704	0.018–0.097	1.538	0.288	4.9211	4.4866	0.20431	0.20658
33	K1	5021 ± 11	4.550	4.18	2.055	0.012–0.050	0.850	0.052	0.0039	0.7731	0.08862	0.11827
34	G9	5485 ± 14	4.557	4.17	2.244	0.013–0.050	0.849	0.073	0.7452	1.2347	0.11311	0.13862
35	G1	5905 ± 15	4.550	4.65	2.547	0.015–0.063	0.933	0.105	1.7012	1.9247	0.13971	0.16830
36	K6	4185 ± 3	4.740	2.70	1.016	0.006–0.025	0.488	0.009	-1.6403	0.3562	0.03898	0.07347
37	K4	4531 ± 10	4.740	2.70	1.140	0.007–0.025	0.539	0.014	-0.8481	0.4077	0.05513	0.09950

*This table is published in its entirety in the electronic edition of the *Astrophysical Journal*.

^aThe simulation numbers are also shown in Fig. 1.

^bThe spectral class is only approximate, as it depends on the luminosity.

^cWidth of the simulation domain, w .

^dDepth of the simulation domain, d .

^eMin. and max. vertical grid-spacing.

^fThe typical granulation size, A_{gran} (See Sect. 4).

^gThe convective expansion of the atmosphere, Λ (See Sect. 3.2).

^hThe unit of entropy is $10^8 \text{ erg g}^{-1} \text{ K}^{-1}$, and the zero-point is specified below Eq. (2).

but is completely determined by the EOS, and the matter is fully mixed, greatly simplifying the analysis.

At the top of convective envelopes, the situation is much more complicated, not the least because it overlaps with the photospheric transition from optical deep (diffusion approximation) to optical thin (free-streaming approximation) and is accompanied by an abrupt change in density gradient. We outline the details below (also see Stein & Nordlund 1989; Nordlund & Stein 1991b, 1997; Nordlund et al. 2009).

The upflows are close to isentropic, rising from the deep interior where convection is adiabatic. They also exhibit only little turbulence, since they are expanding along the exponential density gradient, smoothing out any fluctuations. The smoothing effect gets stronger as the density gradient and velocities increase towards the surface. This density gradient also forces the upflow to

continuously overturn into the downdrafts, in order to conserve mass under the constraint of hydrostatic equilibrium. This overturning occurs with a scale-height of a mass mixing length,

$$\ell_m = |d \ln F_{\uparrow m}(r) / dr|^{-1}, \quad (14)$$

where $F_{\uparrow m}(r)$ is the mass flux, ρu_z , averaged over the upflows only (Trampedach & Stein 2011, TS11). This definition means a fraction of e^{-1} of the upflow will have overturned into the downdrafts over the height interval, ℓ_m . In the deeper parts of our simulations (the same that were analyzed by TS11), below the superadiabatic peak, the mass mixing length is proportional to the pressure scale height, $\ell_m = \alpha_m H_p$ (not the density scale-height, H_ρ , nor the distance to the top of the convection zone, Λ , as has been proposed in the past). We show this in

Fig. 2 for three of our simulations that span our grid.

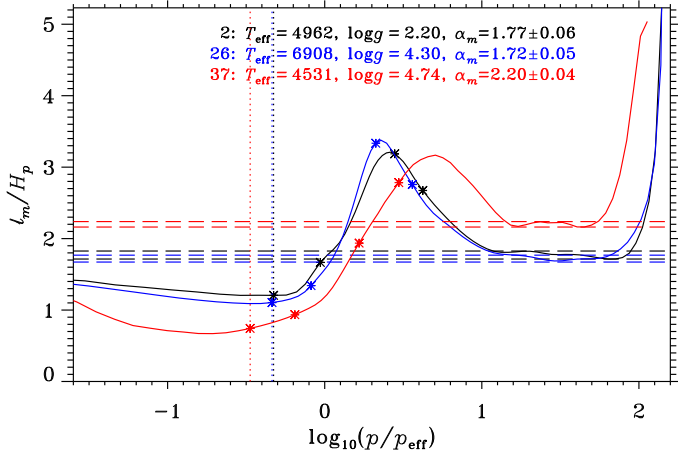


Figure 2. The mass mixing-length, ℓ_m , in units of pressure scale-height, H_p , for three of our simulations (See table 2), as presented by Trampedach & Stein (2011). The abscissa is the logarithmic total pressure normalized by the pressure, p_{eff} , at the depth where $\langle T \rangle = T_{\text{eff}}$. The dashed, horizontal lines show the range of ℓ_m/H_p determined for each of the three simulations. The vertical dotted lines show the location of the top of the respective convection zones. The four asterisks on each curve, show the position of the temperature snapshots shown in Fig. 3.

TS11 finds values of the deep α_m between 1.67 and 2.20. The sharp rise in α_m at the bottom, is due to boundary effects. The mass flux is the quantity displaying the most extreme boundary effects, being further amplified by the differentiation, in this case.

This simple, but powerful concept, of convective flows being dominated by continuous overturning of adiabatic upflows due to mass conservation of flows along a density gradient, is also predictive. At depths where radiative losses are negligible, pure advection of the entropy deficit from surface cooling into an isentropic interior, would result in a local entropy deficit, $S(z) - S_{\text{max}}$, that scales with the density ratio, $\rho(z=0)/\rho(z)$. This is confirmed to high accuracy by the simulations (below $z = 1$ Mm for the solar case).

There is a peak in ℓ_m/H_p about a pressure-decade below the top of the convection zone, before it drops off to about 1 above the photosphere. The top of the convection zone is evaluated as the depth at which the convective flux ($F_{\text{conv}} = F_H + F_{\text{kin}}$, the sum of enthalpy and kinetic fluxes) is zero, and is indicated with the vertical dotted lines in Fig. 2. This point is well-defined since F_{conv} is negative in the overshoot region above the convection zone. For comparison, the superadiabatic gradient peaks around $p/p_{\text{eff}} \sim 1$, straddling the photosphere.

The sharp drop in ℓ_m from its peak value, reflects a change in morphology of the flows. As the mixing-length decreases faster than the pressure scale-height the same upflows have to overturn over a decreasing height-scale, forcing the whole circumference, and not just the vertices, of the upflows to be efficient downflows — this is what we recognize as granulation in the solar photosphere. This granulation pattern is formed in the front side of the mass mixing-length peak, as shown in Fig. 3. Here we show the change of convective morphology with depth, for simulation 37 (sedate convection in a cool

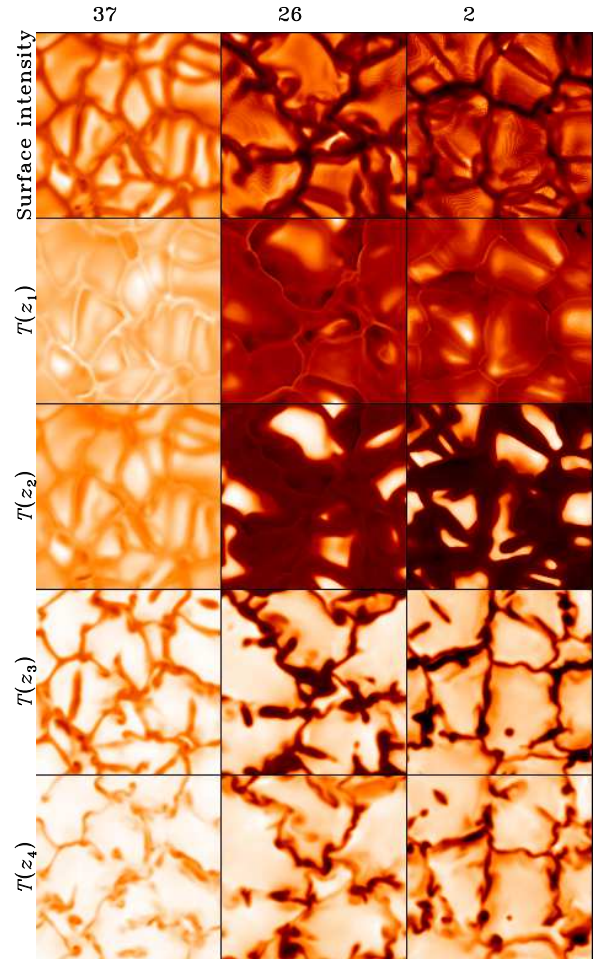


Figure 3. Horizontal planes of temperature for arbitrary snapshots of the three simulations shown in Fig. 2, and at the heights indicated with asterisks in that figure. The top row shows disk-center, white-light intensity. For each row the images are scaled so that contrasts can be directly compared, but the magnitude between simulations can not.

MS dwarf), 26 (vigorous convection in a warm MS star) and 2 (vigorous convection in a red giant). The top row shows the emergent granulation pattern in disk-center, white-light intensity. The third and fourth rows show approximately the top and bottom of the granules and the second and bottom rows show convection six grid-points above and below that, respectively, to illustrate the transition away from granular convection. The displayed quantity is temperature, but it is very similar in internal energy. Vertical velocity, or velocity divergence turned out to be less well suited for finding granules. We (loosely) define the bottom of the granules as where the cooler inter-granular lanes start to disconnect and the downflows concentrate into knots connected by weaker lanes.

In the layer at the top of the granulation (third row) we see all of the granules in the most sedately convective simulation # 37. The most vigorous convection, as seen in # 26, is accompanied by a sharper photospheric temperature drop and we only see a few granules at the peak temperature (brightest in Fig. 3, third row) with the rest of the granules simply peaking in slightly deeper layers. The second row of images shows the morphology at the top of the convection zone, which is characterized

by hot lanes in the middle of inter-granular lanes, and some granules being cooler than these hot lanes at this height. These hot lanes are optically thin, however, and contribute little to the emergent picture of granulation, while the contribution by the granules is just fading, as only the hottest parts of the strongest granules have their photospheres at this height.

The above described formation of granules is a very generic result. Whenever convection takes place in a stratified medium and the mass mixing length undergoes a sudden drop, faster than the pressure scale-height (typically by some form of cooling) a granulation pattern will emerge. It occurs in simulations with simple gray radiative transfer (Kim et al. 1995; Robinson et al. 2003), in simulations with a completely artificial cooling layer and with impenetrable upper boundary (as in the interior convection simulations of, e.g., Miesch et al. 2000; Brun et al. 2004), and it occurs in laboratory experiments with Rayleigh-Bénard convection (Koschmieder 1967; Meyer et al. 1992; Busse & Clever 1998), where the mixing length drops to zero at the surface of the fluid.

In real stellar convection, however, the contrast between the upflows and the downdrafts is controlled by the details of the radiative cooling in the photosphere. This is dominated by the highly temperature sensitive H^- opacity ($\propto T^9$). The isentropic upflows therefore only start cooling very close (spatially) to the unity optical depth. In the cooler downdrafts, on the other hand, unity optical depth occurs much deeper (on a spatial scale) (Georgobiani et al. 2003) and the cooling also occurs over a larger height range. The cooled downflows are also continuously mixed with the high-entropy plasma overturning from the upflows. As they move against the density gradient, the downflows are also turbulent and they contain the majority of vorticity—horizontal at the periphery of downdrafts and vertical in the centers. This inherent asymmetry between the upflows and the downdrafts makes it rather difficult to treat in analytical 1D formulations. The asymmetry also results in density differences between upflows and downdrafts, which gives rise to a kinetic energy flux which is negative and increasing to about 20% of the total flux at the bottom of our simulation domains. This kinetic flux is not accounted for in MLT formulations, but together with the enthalpy flux makes up the convective flux in the simulations. There are also 5–13% contributions from acoustic fluxes inside the convection zone (largest for cool giants) and minor viscous fluxes that peak at less than 1%, just below the superadiabatic peak. The density difference in turn implies a difference in filling factor between the up- and downflows (assuming hydrostatic equilibrium as realized to a large extent by the simulations). The filling factor is about 60% of the area being in the upflows in the deep parts, fairly constantly with height and atmospheric parameters. It changes abruptly at the top of the convection zone, to be a bit below 50% above the photosphere.

3.1. Convective Efficiency

The efficiency of convection is intimately connected to the convective velocities and the temperature and density contrasts. A larger atmospheric entropy jump (a larger superadiabatic peak) means less efficient convection, as the deviation from an adiabat implies energy

losses on the way. The ideally efficient convection would not lose any energy before reaching the top of the convection zone. Comparing two cases with differing efficiency, but same total flux, the less efficient will necessarily have higher convective velocities in order to transport the same flux. These larger vertical velocities also means larger horizontal, overturning velocities between the upflows and the downdrafts, sustaining larger pressure contrast between the two. The entropy jump is set up by increased cooling around the photosphere, which drives a larger temperature contrast between the upflows and the downdrafts (and therefore also a larger emergent intensity contrast between granules and inter-granular lanes, as seen in Fig. 11). This entropy jump is shown in Fig. 4 for our grid of simulations (also see Trampedach 2012).

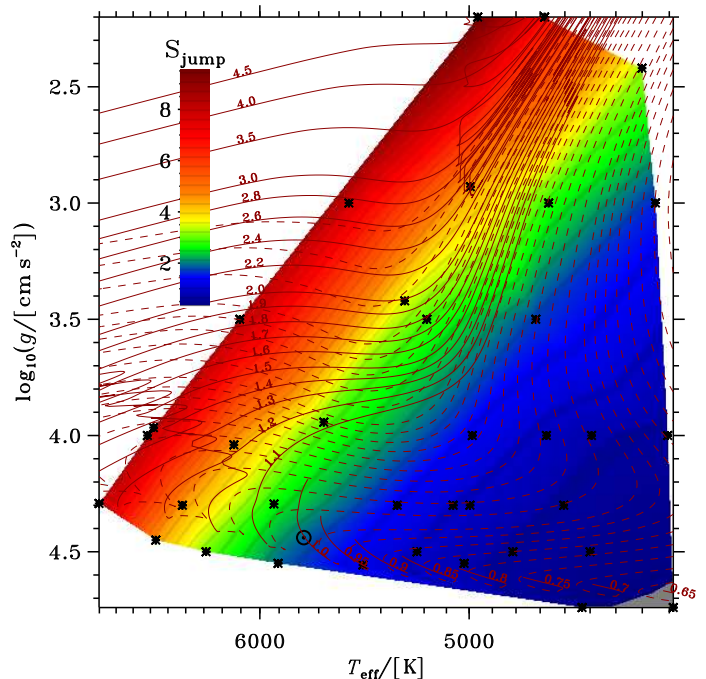


Figure 4. As Fig. 1, but showing the atmospheric entropy jump $S_{\text{jump}}/[10^8 \text{ erg g}^{-1} \text{ K}^{-1}]$, a measure of convective efficiency, as function of stellar atmospheric parameters.

We clearly see that cool dwarfs have the most efficient convection and it gets progressively less efficient as the limit of convective envelopes is approached (a diagonal in the plot, above the high- T_{eff} /low- g limit of our grid). Beyond this limit no significant flux is transported by convection near the surface. Comparing with the asymptotic adiabat shown in Fig. 1 (or the turbulent pressure ratio in Fig. 6), we see a very similar behavior, although the entropy jump falls off faster as the limit of convective envelopes is approached. In terms of MLT formulations, a large convective efficiency is accomplished with a large mixing length, which carries entropy further before mixing with the surroundings.

Two stars that are otherwise similar (in effect, the same $\log g$ and asymptotic entropy, S_{max}), but have different atmospheric opacities, will also have different convective efficiencies. The radiative loss of energy around the photosphere, will happen in the same range of optical depth, for the two stars, but for the star with lower opacity this range will correspond to a larger range in (spatial)

depth, as $d\tau = \rho\kappa dz$. With similar convective velocities, this would lead to more time spent losing energy to the radiation field, and consequently increasing the atmospheric entropy jump and hence, decreasing the convective efficiency. A lower efficiency leads to higher velocities, which will limit the radiative losses above, providing a negative feed-back and enabling an equilibrium state. The net flux and therefore T_{eff} will most likely be affected by such an opacity change. One reason for lower atmospheric opacities, is of course a lower metallicity, which would then be expected to result in lower convective efficiency. We do not explore variation in metallicity with our grid of simulations, but a recent investigation of solar like Kepler stars by Bonaca et al. (2012), finds a decreasing α with decreasing metallicity, as argued above. This opacity effect on convection is, of course, also relevant for assessing effects of opacity updates on models or of how composition altering processes could affect stars and maybe explain observations.

3.2. Seismology and Surface Convection

The so-called surface effect (Christensen-Dalsgaard & Thompson 1997), is a systematic and persistent difference between observed and model frequencies, which is independent of the degree, l , of the modes. This surface effect is caused by differences between the star and the model in the layers around the upper turning-point of the p modes. This is also the layers where the photospheric transition from optical deep (diffusion approximation) to optical thin (free streaming), and the transition at the top of the convection zone from convective to radiative transfer of the flux, occur. The latter results in the most inefficient convection in that star, with large velocities, large turbulent pressure, large temperature fluctuations and the most superadiabatic convection. The photospheric transition enhances the convective fluctuations by rapid cooling of the upflows. All these effects, and the strong coupling between radiation and convection, means that a 1D, plane-parallel, MLT atmosphere is an inadequate description. Most of the assumptions that MLT build on are violated in this region and we therefore expect, and have seen, large systematic differences between observed and model p mode frequencies. Since the problems occur in a thin layer around the upper turning point, all modes feel it equally, and the frequency differences are therefore mainly a function of frequency. The usual procedure is therefore to adjust the model frequencies by a smoothly varying function of frequency. This procedure seems to work well for then Sun, and has also been applied successfully to other stars Kjeldsen et al. (2008).

The main reason for the surface effect is a convective expansion of the atmosphere, which enlarges the acoustic cavity of the modes. This expansion is shown in Fig. 5 for the grid of simulations. It is evaluated as the average outward shift of the (total) pressure stratification between $\langle \ln p_{\text{tot}} \rangle_L$ of each simulation and their corresponding 1D stellar envelope model, from their respective photospheres and up. The 1D models are based on the same EOS and opacities, and have been matched to the averaged simulations, thereby calibrating the mixing-length parameter, α (Trampedach et al. 2013). This ensures the 3D and 1D models are comparable, with the only major difference being the treatment of convection.

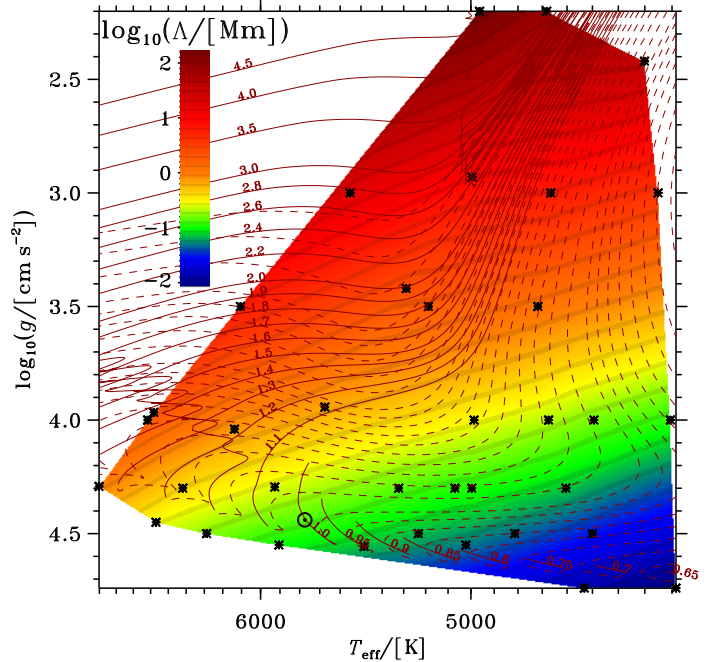


Figure 5. As Fig. 1, but showing the logarithmic total convective expansion of the atmosphere, Λ_{conv} , as function of stellar atmospheric parameters.

About half of this expansion is due to the turbulent pressure contributing to the hydrostatic support. The maximum of the turbulent- to total-pressure ratio is shown in Fig. 6, and is found to depend on atmospheric parameters in a similar way as the entropy of the asymptotic adiabat in Fig. 1. Fig. 6 spans pressure ratios from 3.90% for the coolest dwarf to 29.6% for the warmest giant (closely followed by 27.6% for the hottest dwarf in our grid). From the different T_{eff} and $\log g$ dependencies in Figs. 5 and 6 it is clear that it is not the pressure ratio itself that determines the atmospheric expansion. As we did for Eq. (12), we invert the equation of hydrostatic equilibrium and now integrate over just the turbulent component of the pressure, to get the associated expansion

$$\Lambda_{\text{turb}}(z) = \int_{P_{\text{turb}}(z_{\text{bot}})}^{P_{\text{turb}}(z)} \frac{dP_{\text{turb}}(z')}{g\varrho(z')} . \quad (15)$$

The total pressure is composed of, e.g., $P = P_{\text{rad}} + P_{\text{gas}} + P_{\text{turb}}$, and the gas pressure can be further decomposed into contributions by individual elements, ions, electrons or molecules. The amount of atmospheric expansion by any of those pressure components can be computed in the same way as that by the turbulent pressure, in Eq. (15) above. The integration is carried out from the interior to the top of the domain. About half of Λ_{turb} (\sim quarter of the full Λ_{conv}) is actually supplied by the overshoot region above the convection zone, which in most 1D MLT models has no velocity fields.

This turbulent component provides approximately half of the full expansion shown in Fig. 5. The rest is due to the so-called *convective back-warming* (Trampedach 2002, Paper I), which is caused by the large convective temperature fluctuations in the photosphere, combined with the high temperature sensitivity of the opacity there ($\kappa(\text{H}^-) \propto T^9$). This effectively limits the radiative losses

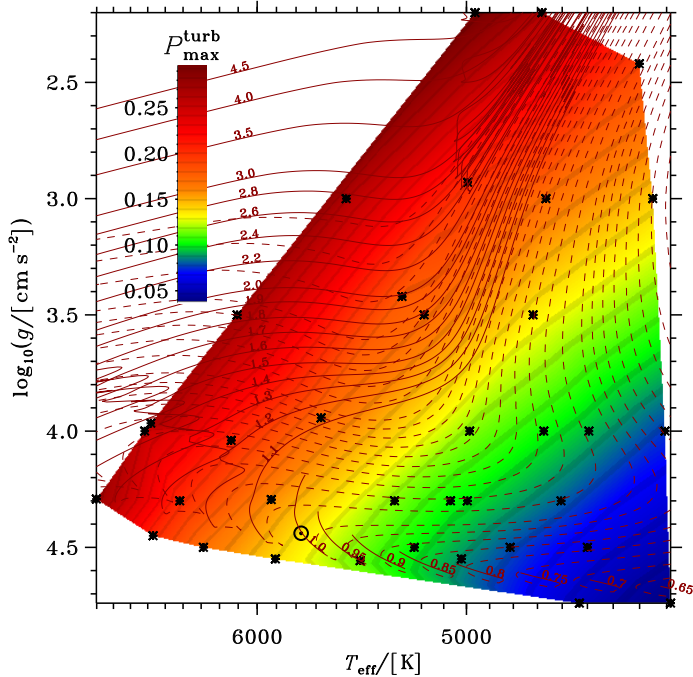


Figure 6. As Fig. 1, but showing the maximum (with depth) of the $P_{\text{turb}}/(P_{\text{turb}} + P_{\text{gas}})$ -ratio, as function of stellar atmospheric parameters.

from the hot granules, to a larger extent than would have been the case for a corresponding 1D model with the average temperature stratification. Because the temperature fluctuations are well past the linear regime of the opacities, the effect is not symmetrically opposite in the cooler inter-granular lanes, and a net back-warming results, akin to the effect of line-blanketing (Gustafsson et al. 2008, Sect. 6.1). The back-warming results in a larger (gas) pressure scale-height, i.e., an expansion of the atmosphere.

Rosenthal et al. (1999) found the expansion of the solar atmosphere, relative to a 1D MLT model, to be a major ingredient of the surface effect. The effective gradient of the turbulent pressure, $\gamma_{1,\text{turb}}$ (Stein & Nordlund 1991), however, was found to be of similar importance. We show the inverse of this, $d \ln \rho / d \ln p_{\text{turb}}$ for the solar simulation in Fig. 7. From the top panel of this plot, we see how $\langle p_{\text{turb}}(t) \rangle_{\text{L}}$ vs. $\langle \rho(t) \rangle_{\text{L}}$ displays a great deal of scatter, increasing with height above the photosphere. Despite this, a linear fit at each height is well-defined and gives a rather steep positive gradient above the photosphere, going through vertical in the photosphere (the reason we show $1/\gamma_{1,\text{turb}}$ in the bottom panel), and being steep and negative in the interior, converging towards vertical (with minimal scatter). The shape of $1/\gamma_{1,\text{turb}}$ is rather universal for our simulations, mainly varying in the amplitude of the various components of the curve.

The appropriate form of the total γ_1 can be gleaned from the manner in which γ_1 enters the oscillation equations. From Eq. (1) of Christensen-Dalsgaard (2008) we see that γ_1 only enters through terms similar to the first term on the right-hand-side of Eq. (16)

$$\frac{1}{\gamma_{1,\text{tot}}} \frac{d \ln p}{d \ln r} \equiv \frac{1}{\gamma_1} \frac{d \ln p_{\text{g}}}{d \ln r} + \frac{1}{\gamma_{1,\text{turb}}} \frac{d \ln p_{\text{turb}}}{d \ln r}, \quad (16)$$

and we propose the total γ_1 to be given by the left-hand-

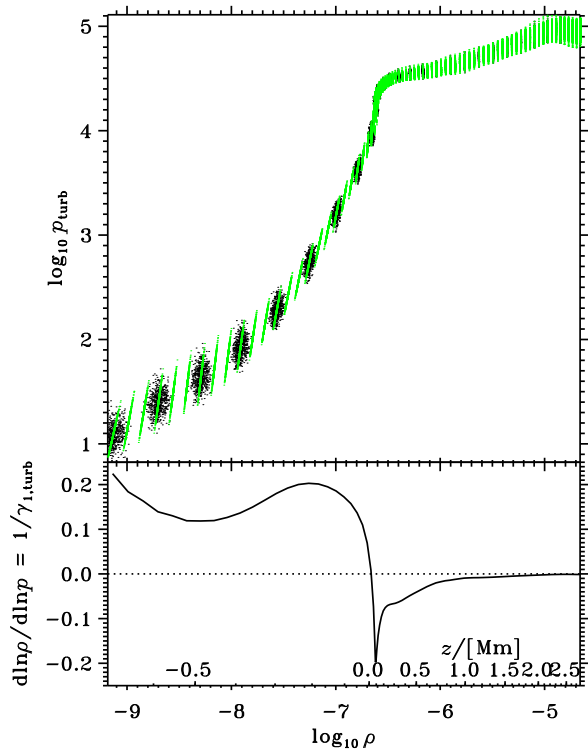


Figure 7. Top panel: Black points show horizontally averaged $\langle p_{\text{turb}}(t) \rangle_{\text{L}}$ vs. $\langle \rho(t) \rangle_{\text{L}}$ for each snapshot of the solar simulation time-series (for every third depth-point). The green lines show linear fits to these points, at each depth. **Bottom panel:** Inverse gradients of the fits from the top panel, as function of depth (upper axis) and density (lower axis, in common with the top panel).

side. Such a $\gamma_{1,\text{tot}}$ requires a knowledge of the total pressure, $p_{\text{g}} + p_{\text{turb}}$. We can also define a total γ_1 that gives the response in the total pressure, based on just the gas pressure

$$\tilde{\gamma}_{1,\text{tot}} \equiv \frac{d \ln p_{\text{g}}}{d \ln r} / \left[\frac{1}{\gamma_1} \frac{d \ln p_{\text{g}}}{d \ln r} + \frac{1}{\gamma_{1,\text{turb}}} \frac{d \ln p_{\text{turb}}}{d \ln r} \right]. \quad (17)$$

We show this expression together with the pure gas γ_1 for our solar simulation, in Fig. 8. The reduced γ_1 , adopted by Rosenthal et al. (1999) as a limiting case

$$\gamma_{1,\text{red}} = \gamma_1 \frac{p_{\text{g}}}{p_{\text{g}} + p_{\text{turb}}}, \quad (18)$$

is also shown in Fig. 8, and is rather different from our Eq. (17). Rosenthal et al. (1999) found that using the gas γ_1 for both pressures gave frequencies closer to the observed solar ones, than using Eq. (18). With the rather different behavior of Eq. (17), there is a potential for improved agreement with helioseismic observations, when using Eq. (17).

This calculation is only a first step, since it assumed no phase-lag between density and turbulent pressure, and since we assumed $\gamma_{1,\text{turb}}$ to be independent of frequency. Future work with our grid of simulations will address these very important issues, which has grown more urgent with the advances in asteroseismology and the recent results by Mathur et al. (2012). They studied 22 solar-like stars, targeted by NASA's Kepler mission, and found magnitudes of the surface effect that are not immediately reconcilable with Fig. 5, suggesting that $\gamma_{1,\text{turb}}$ -effects are significant.

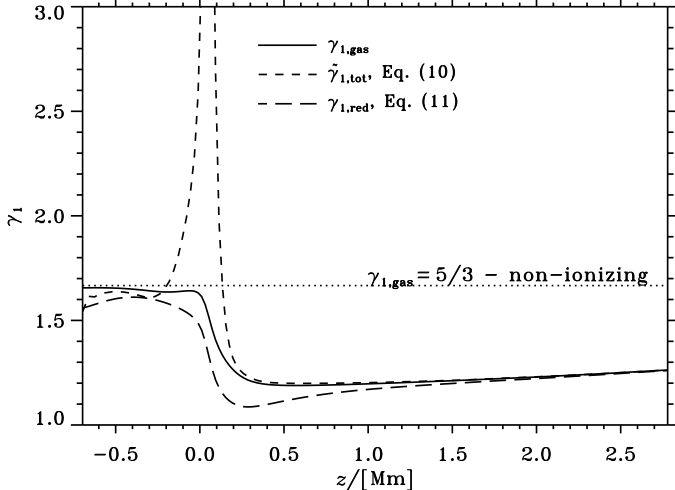


Figure 8. The total γ_1 , including both thermo- and hydrodynamic effects, for the solar simulation of our grid. The peak in $\tilde{\gamma}_{1,\text{tot}}$ reaches a value of 5.46.

4. VARIATION OF GRANULATION WITH STELLAR PARAMETERS

In this section we present the variation of granulation size and intensity contrast with respect to the dependent variables of the grid, T_{eff} and $\log g$. In the case of our own star, the sizes of granules can be measured directly from both ground- and space-based observations, and agree well with simulations. The intensity contrast, on the other hand, is less well constrained as observations are affected by both seeing, limited aperture, diffraction and scattering from various parts of the telescope, focus issues, etc., that can easily halve the observed contrast. Attempting to model these effects in Hinode observations, Danilovic et al. (2008) found general agreement with their MuRAM simulations, with which ours agree fairly well. We find a 16.3% RMS fluctuation in white light granulation for our solar simulation, compared to their 14.4% RMS contrast in 6300 Å monochromatic light. Beeck et al. (2012) shows that the 5000 Å contrast agrees between the simulations, although the detailed distribution and granulation patterns do differ some.

It is worth noting that granulation in many ways are more constrained by unresolved spectral observations (Nordlund et al. 2009), as can also be carried out for stars. This is due to the fact that convection in late-type stars sets up correlations between temperature and velocity, which results in C-shaped bisectors of emergent spectral lines (Gray 1982; Baştürk et al. 2011). The detailed line shapes of our solar and Procyon simulations agree well with observations (Asplund et al. 2000b; Allende Prieto et al. 2002).

4.1. Intensity Distribution of Granulation

We have calculated 2D spatial power spectra of the white light, disk center, surface intensity for each of the simulations, and averaged the spectra over time (at least 10 periods of the fundamental p mode excited in each simulation). These spectra are very broad, as can be seen from Fig. 9, but the maxima, marked by filled circles and defining the typical size of granulation, is never-the-less

well-defined. The range of each spectrum reflects the horizontal resolution at the lower end, and the horizontal extent at the upper end. The similar relative location of the peak in each spectrum means the granules are similarly well resolved. This granular size, A_{gran} , is pre-

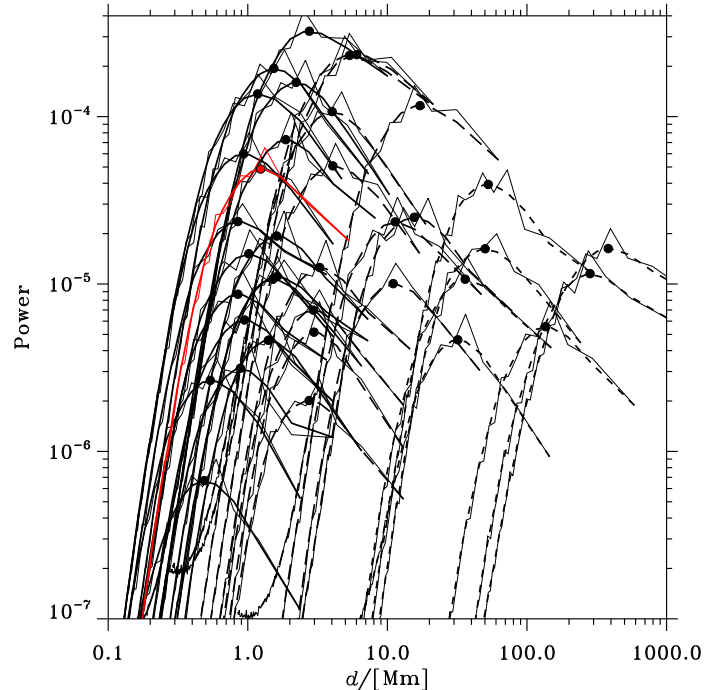


Figure 9. The time averaged spatial spectra of emergent disk-center intensity for each of the simulations of the grid. The thin lines are the raw spectra, and the thick lines are the spectra smoothed with a Gaussian kernel with FWHM of 11 wavenumber points. We used short-dashed lines for giants ($\log g < 2.1$), long-dashed lines for turn-off stars and solid lines for dwarfs ($\log g > 4.1$). The solar simulation is shown in red. The abscissa, $d = 2/(\sqrt{\pi}k)$, refers to diameters of circles with the same area as the $1/k^2$ square, where k is the wavenumber corresponding to the Fourier transform. The maxima of the smoothed spectra are indicated with circles, and the corresponding granular sizes, A_{gran} , are listed in table 2. The transformation of the maxima to the atmospheric HR-diagram, Fig. 10, is bijective, with giants to the right and cool dwarfs at the lower left.

sented in Fig. 10. The granular size, A_{gran} , grows almost inversely proportional with the surface gravity and increases only slightly with T_{eff} . A least squares fit results in

$$\log \frac{A_{\text{gran}}}{[\text{Mm}]} \simeq (1.3210 \pm 0.0038) \times \log T_{\text{eff}} - (1.0970 \pm 0.0003) \times \log g + 0.0306 \pm 0.0359, \quad (19)$$

where g is in cgs-units and the 1σ uncertainties of the linear regression is indicated. So the sensitivity to T_{eff} is slightly larger than to $\log g$, but since the stellar range of T_{eff} is so much smaller than the range in gravity, the gravity dependence is effectively the most important, as also seen in Fig. 10. It is often speculated that the size of granules scales with the pressure scale-height (Schwarzschild 1975) or the mixing length in the atmosphere, but we find such factors ranging from $A_{\text{gran}}/H_p \sim 9\text{--}13$ and $A_{\text{gran}}/(\alpha H_p) \sim 5\text{--}9$, respectively, both generally increasing from dwarfs to giants.

The time-averaged histograms of surface intensities has

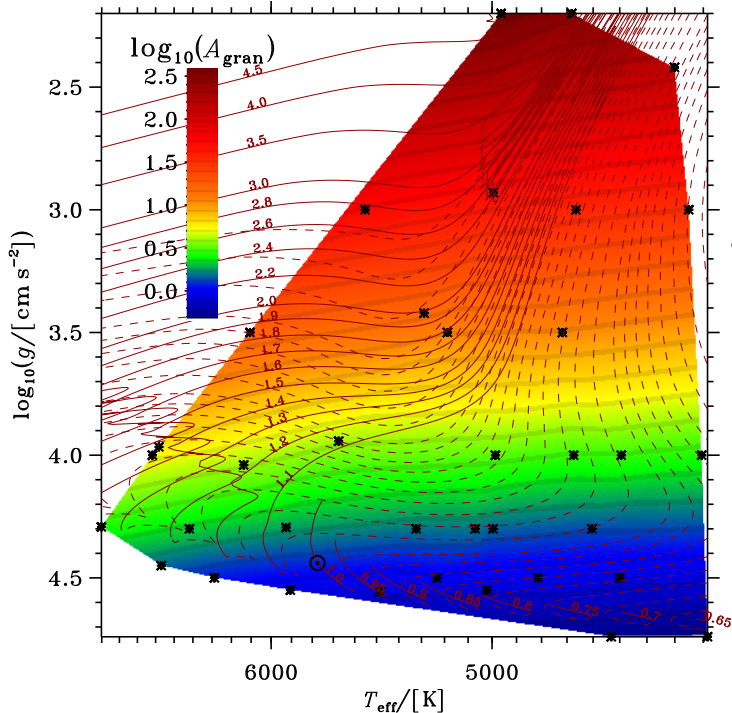


Figure 10. The typical size of granulation (logarithmic scale) as function of atmospheric parameters. The granular size is found as the maxima of the smoothed spectra in Fig. 9.

a bi-modal structure, with most of the surface being covered in bright upflows with a narrower distribution of intensities than the less bright, inter-granular lanes.

The intensity distributions of granules are narrower, due to the upflows being nearly isentropic (See Sect. 3). Their widths are determined by the radiative losses suffered by the over-turning upflows at the top of the convective envelope. If the top is located in optically deep layers, the radiative losses will be relatively minor and both the width of the intensity distribution of the granules, and the intensity contrast of the inter-granular lanes are small—The granulation is largely hidden from our view.

If the granulation reaches into optically thin layers, on the other hand, the reverse is the case and we see both a broader distribution and a larger contrast. This is often referred to as “naked granulation”, a term coined by Nordlund & Dravins (1990).

The down-flows, on the other hand, are darker and have a much broader distribution. These intensity distributions are well-approximated by a simple double Gaussian

$$n(I) = I_1 e^{-((I-I_2)/I_3)^2} + I_4 e^{-((I-I_5)/I_6)^2}. \quad (20)$$

Fits to that expression are displayed in Fig. 12. Here we also notice that the simulations display less of a dip between the two components, compared to the double Gaussian fit. This third component, is due to the breaking up of granules, which occurs in most of the snapshots shown here. Some of the granules gets split apart by wedges of cool down-flows, others, mainly the largest granules, have cool spots developing in their centers, suddenly succumbing to the negative buoyancy and turning into a down-draft. This occurs when the upflow in a granule (proportional to the area of the granule) exceeds the

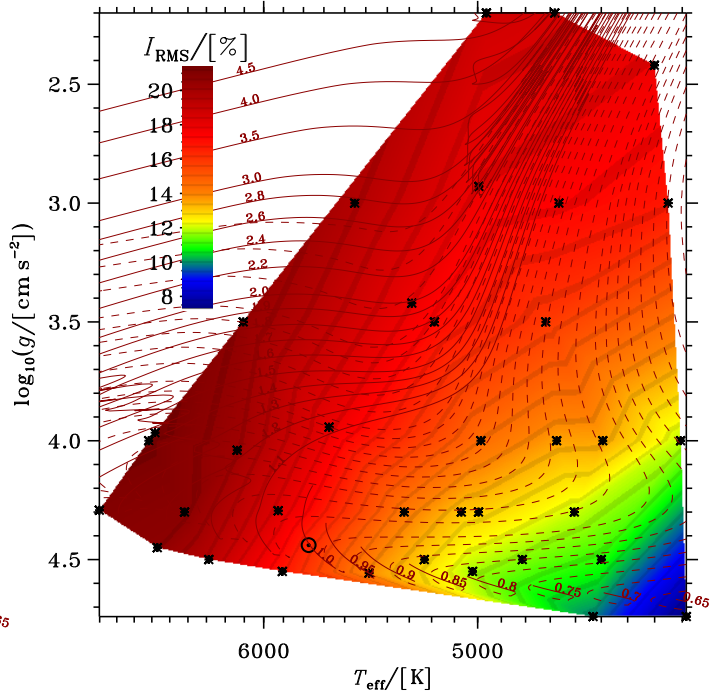


Figure 11. As Fig. 1, but showing the contrast of granulation, evaluated as the RMS scatter of the normalized intensity, $I/\langle I \rangle$.

capacity for horizontal outflow from the granule (proportional to the circumference), braking the upflow and thus increasing the cooling time. The developing cool spot, quickly connects to the nearest inter-granular lane. This phenomenon is also known as *exploding granules* (Namba & van Rijsbergen 1977; Spruit et al. 1990; Nordlund & Stein 1991a), although “exploding” seems a bit dramatic for all, but the largest of these events. (See, e.g., Rast 1995, for comparisons of simulations and observations of exploding granules).

The granulation in the snapshots of Fig. 12 looks rather different between the simulations, but this is a random occurrence, and the morphology looks different for another set of snapshots of the same simulations (cf. Fig. 3 for different snapshots of simulations 2, 26 and 37). The over-all scale of the granulation is not apparent in Fig. 12 as the dimensions of each simulation is chosen so as to contain a similar number of granules (about 30 granules), and the only property that varies markedly and systematically with atmospheric parameters, is the intensity contrast. We note that the distribution appears bimodal for only the higher gravity simulations. For the two giants of Fig. 12, however, the distributions are not symmetric and they are still best described by two separate Gaussians, as in Eq. (20). It is interesting that it is rather hard to pick out the intensity distribution from the picture. One might recognize sharper edges in the granules of simulation #26, compared to that of #4, which gives rise to the separation of the two components in the distribution, but it is not immediately obvious that, e.g., the two giants are similar. We also note that the unfitted component from splitting or “exploding” granules, increases with surface gravity, to the point of being absent in the simulations of giants. This behavior is not yet understood.

The contrast of the granulation, evaluated as the RMS

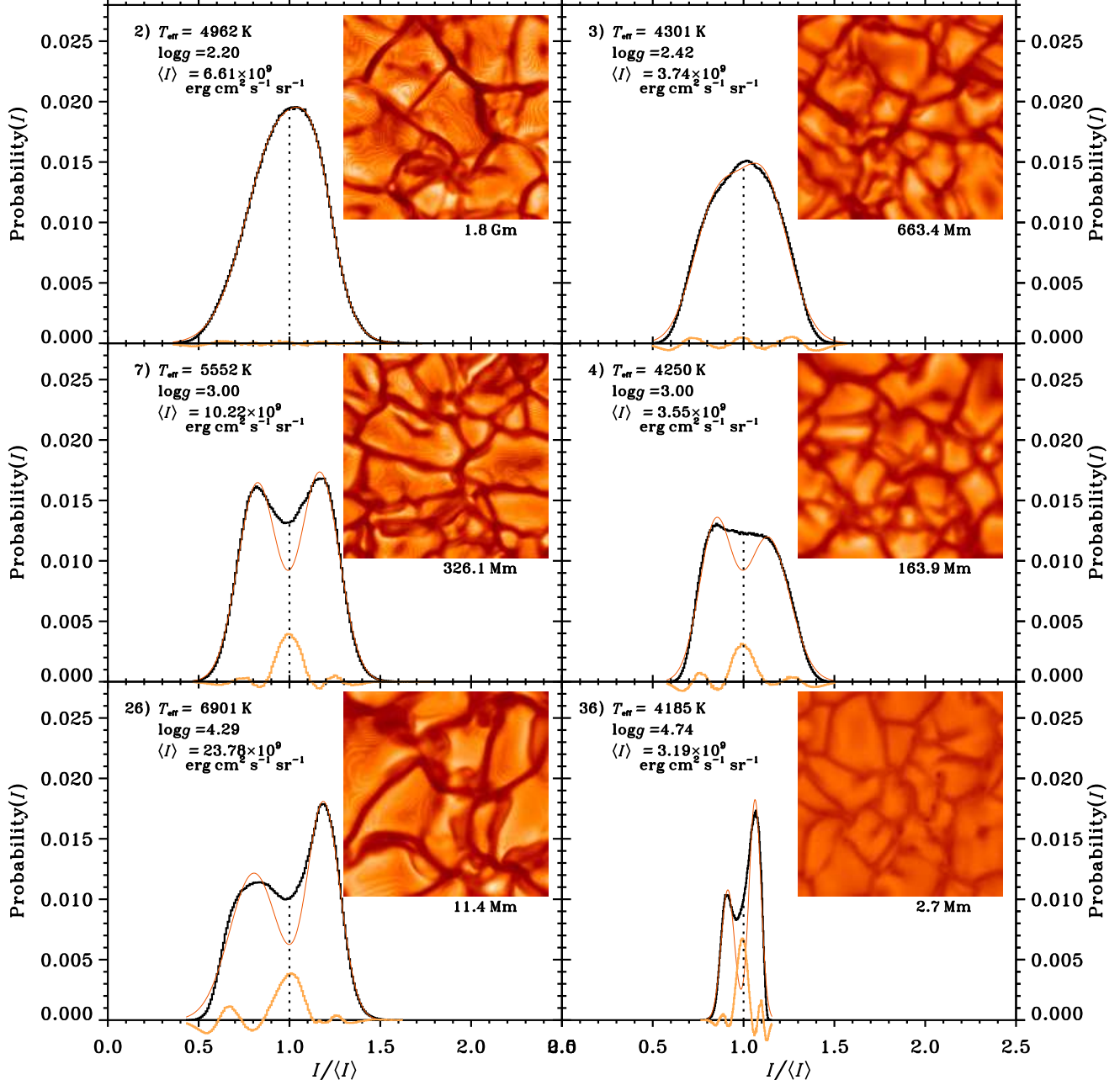


Figure 12. The intensity distributions of each of the simulations of the grid (black histogram), together with a fit to Eq. (20) (thin orange line) and the difference between the two in yellow. From the differences we see a third component, increasing with gravity. The abscissa shows intensity normalized to the average for each simulation, to facilitate comparisons. This average intensity is listed together with the atmospheric parameters, in each panel. We also display white light, disk-center, surface intensity snapshots, with the horizontal extent of each simulation indicated below. The displayed snapshots were chosen to have intensity distributions close to the average for each simulation.

scatter around the mean is shown in Fig. 11. From this figure we see how the contrast behaves similarly to the convective efficiency, as measured by the atmospheric entropy jump, Fig. 4, with the highest contrast for the least efficient convection. The slope of iso-contrast lines change significantly from the cool to the warm side of the diagram, as opposed to the near-constant slopes of the entropy jump. The granulation contrast increases rather linearly across the contours, whereas the entropy jump increases close to exponentially, as function of $\log T_{\text{eff}}$ and $\log g$.

On the main sequence, for $\log g \geq 4$, a linear fit to the

intensity contrast gives

$$I_{\text{RMS}}/[\%] = (54.98 \pm 1.86) \times \log T_{\text{eff}} - (4.80 \pm 0.53) \times \log g - 169.00 \pm 0.73, \quad (21)$$

and towards the giants, for $\log g \leq 3$,

$$I_{\text{RMS}}/[\%] = (20.81 \pm 1.34) \times \log T_{\text{eff}} - (1.11 \pm 0.14) \times \log g - 55.46 \pm 0.29. \quad (22)$$

Notice the change of $\log T_{\text{eff}}$ - and $\log g$ -dependency between dwarfs and giants, recognized as the change of

slope of the contours in Fig. 11.

5. CONCLUSIONS

We present an attempt at constructing a homogeneous, comprehensive, grid of 3D convective atmosphere simulations, with derived quantities for use by the general astronomical community. The simulations are constructed to be as realistic as possible, with realistic EOS, opacities and radiative transfer, in order to provide a solid foundation for interpreting observations.

For all the subjects studied in the present paper, we found significant differences with respect to conventional 1D stellar atmosphere models—differences that will have an impact on the interpretation of most stellar observations.

In Sect. 3 we gave an overview of the nature and morphology of convection, as observed in the simulations of our grid. We see fast, turbulent, entropy deficient downdrafts, driven by radiative cooling at the surface, plowing through an ambient, isentropic, laminar upflow. This is rather different from the picture normally associated with the MLT formulation, of distinct, warm, rising convective elements, existing for a mere mixing-length. We hope that the more realistic concept of convection, based on hydrodynamic simulations, will provide an improved framework for further theoretical developments in simplified, but realistic, descriptions of convection.

Components of the seismic surface effect, a systematic frequency shift of observed p modes compared to 1D stellar model predictions, were explored in Sect. 3.2. Part of the effect is due to enlarged acoustic cavities, caused by a convective expansion of the atmosphere (with respect to 1D models). This expansion depends smoothly on atmospheric parameters, ranging from 8.7 km for the coolest dwarf in our grid, 140 km for the Sun, to 170 Mm for the warmest giant. We also attempt to derive an effective adiabatic gradient for the turbulent pressure, which is another important component of the surface effect. This $\gamma_{1,\text{turb}}$ behaves rather differently from previous assumptions about its properties. From the form of the adiabatic oscillation equations, we propose the effective γ_1 should be a harmonic mean, weighted by the pressure gradients, Eq. (16).

Convection manifests itself as granulation at the surface, but has only been directly observed for the Sun. In Sect. 4, we find that the size depends smoothly on atmospheric parameters, but is not simply proportional to atmospheric pressure scale-height, as has often been assumed for a lack of observational constraints.

We have shown that employing realistic 3D convection simulations in the interpretation of stellar observations will affect all stages of the analysis, and also allow new questions to be asked—questions that have been beyond simplified, 1D models of convection. In the near future our grid of simulations will be used for calibrating the MLT mixing-length, and evaluate the excitation and damping of p modes, among other applications.

The helpful comments and suggestions by the anonymous referee are much appreciated. We are grateful to W. Däppen for access to the code and data tables for the MHD equation of state. RT acknowledges funding from the Australian Research Council (grants DP 0342613

and DP 0558836) and NASA grants NNX08AI57G and NNX11AJ36G. ÅN acknowledges current support from the Danish Natural Science Research Council and from the Danish Center for Scientific Computing (DCSC). RFS acknowledges NSF grant AGS-1141921 and NASA grant and NNX12AH49G. This research has made extensive use of NASA's Astrophysics Data System.

REFERENCES

- Abramowitz, M., & Stegun, I. A., eds. 1964, Applied Mathematics Series, Vol. 55, Handbook of Mathematical Functions, 2nd edn. (National Bureau of Standards)
- Allende Prieto, C., Asplund, M., López, R. . G. ., & Lambert, D. L. 2002, *ApJ*, 567, 544
- Anders, E., & Grevesse, N. 1989, *Geochim. Cosmochim. Acta*, 53, 197
- Asplund, M., Grevesse, N., Sauval, A. J., & Scott, P. 2009, *ARAAS*, 47, 481
- Asplund, M., Grevesse, N., & Sauval, J. 2005, in *Cosmic abundances as records of stellar evolution and nucleosynthesis*, ed. T. G. Barnes III & F. N. Bash, ASP Conf. Ser. No. 336 (San Francisco: ASP), 25–38
- Asplund, M., Ludwig, H.-G., Nordlund, Å., & Stein, R. F. 2000a, *A&A*, 359, 669
- Asplund, M., Nordlund, Å., Trampedach, R., Allende Prieto, C., & Stein, R. F. 2000b, *A&A*, 359, 729
- Baglin, A., Auvergne, M., Catala, C., et al. 2002, in *Radial and Nonradial Pulsations as Probes of Stellar Physics*, ed. C. Aerts, T. R. Bedding, & J. Christensen-Dalsgaard, IAU Coll. 185, ASP Conf. Ser. No. 259, 626
- Baştürk, Ö., Dall, T. H., Collet, R., Curto, G. L., & Selam, S. O. 2011, *A&A*, 535, A17:12pp
- Basu, S. 1998, *MNRAS*, 298, 719
- Basu, S., & Antia, H. M. 1995, *MNRAS*, 276, 1402
- Beck, B., Collet, R., Steffen, M., et al. 2012, *A&A*, 539, A121:11pp
- Bell, K. L. 1980, *J. Phys. B*, 13, 1859
- Bell, K. L., & Berrington, K. A. 1987, *J. Phys. B*, 20, 801
- Böhm-Vitense, E. 1958, *Zs. f. Astroph.*, 46, 108
- Bonaca, A., Basu, S., Tanner, J. D., et al. 2012, *ApJ*, 755, L12:7pp
- Borucki, W. J., Koch, D., Basri, G., et al. 2010, *Science*, 327, 977
- Broad, J. T., & Reinhardt, W. P. 1976, *Phys. Rev. A*, 14, 2159
- Brun, A. S., Miesch, M. S., & Toomre, J. 2004, *ApJ*, 614, 1073
- Bruntt, H., Kjeldsen, H., Buzasi, D. L., & Bedding, T. R. 2005, *ApJ*, 633, 440
- Busse, F. H., & Clever, R. M. 1998, *Phys. Rev. Lett.*, 81, 341
- Butler, K., & Zeppen, C. J. 1990, *A&A*, 234, 569
- Canuto, V. M., & Mazzitelli, I. 1991, *ApJ*, 370, 295
- . 1992, *ApJ*, 389, 724
- Castelli, F., & Kurucz, R. L. 2003, in *Modelling of Stellar Atmospheres*, ed. N. Piskunov, W. W. Weiss, & D. F. Gray, IAU Symp. No. 210 (ASP), A20
- Christensen-Dalsgaard, J. 2008, *Ap&SS*, 316, 113
- Christensen-Dalsgaard, J., & Thompson, M. J. 1997, *MNRAS*, 284, 527
- Collet, R., Magic, Z., & Asplund, M. 2011in , 012003
- Danilovic, S., Gandorfer, A., Lagg, A., et al. 2008, *A&A*, 484, L17
- Däppen, W., & Gough, D. O. 1984, in *Theoretical Problems in Stellar Stability and Oscillations*, Liège Int. Astroph. Coll. No. 25, 264–268
- Däppen, W., Mihalas, D., Hummer, D. G., & Mihalas, B. W. 1988, *ApJ*, 332, 261
- Däppen, W., & Nayfonov, A. 2000, *ApJS*, 127, 287
- Dawes, W. R. 1864, *MNRAS*, 24, 161
- Dravins, D., & Nordlund, Å. 1990, *A&A*, 228, 184
- Feautrier, P. 1964, in *Proceedings of the First Harvard-Smithsonian Conference on Stellar Atmospheres*, ed. E. H. Avrett, O. Gingerich, & C. A. Whitney, SAO Special Report No. 167 (Cambridge: SAO), 80–82
- Freytag, B., Steffen, M., Ludwig, H.-G., et al. 2012, *J. Comp. Phys.*, 231, 919
- Gavrila, M. 1967, *Phys. Rev.*, 163, 147
- Georgobiani, D., Stein, R. F., & Nordlund, Å. 2003, *ApJ*, 596, 698

- Gray, D. F. 1982, *ApJ*, 255, 200
- Grevesse, N., & Sauval, A. J. 1998, *Space Sci. Rev.*, 85, 161
- Gustafsson, B. 1973in (Uppsala: Landstingets Verkstäder), 1–31
- Gustafsson, B., Bell, R. A., Eriksson, K., & Nordlund, Å. 1975, *A&A*, 42, 407
- Gustafsson, B., Edvardsson, B., Eriksson, K., et al. 2008, *A&A*, 486, 951
- Hauschildt, P. H., Allard, F., & Baron, E. 1999a, *ApJ*, 512, 377
- Hauschildt, P. H., Allard, F., Ferguson, J., Baron, E., & Alexander, D. R. 1999b, *ApJ*, 525, 871
- Hayek, W., Asplund, M., Carlsson, M., et al. 2010, *A&A*, 517, A49
- Herschel, W. 1801, *Phil. Trans. R. Soc.*, 91, 265
- Hummer, D. G., & Mihalas, D. 1988, *ApJ*, 331, 794
- Hyman, J. M. 1979, in *Adv. in Comp. Meth. for PDE's*, ed. R. Vichnevetsky & R. S. Stepleman, Vol. 3 (New Brunswick: IMACS), 313–321
- Kim, Y.-C., Fox, P. A., Sofia, S., & Demarque, P. 1995, *ApJ*, 442, 422
- King, J. I. F. 1956, *ApJ*, 124, 406
- Kjeldsen, H., Bedding, T. R., & Christensen-Dalsgaard, J. 2008, *ApJ*, 683, L175
- Koschmieder, E. L. 1967, *J. Fluid Mech.*, 30, 9
- Kurucz, R. L. 1992a, *Rev. Mex. Astron. Astrofis.*, 23, 45
- . 1992b, *Rev. Mex. Astron. Astrofis.*, 23, 181
- Kurucz, R. L., van Dishoeck, E. F., & Tarafdar, S. P. 1987, *ApJ*, 322, 992
- Langhoff, P., Sims, J., & Corcoran, C. T. 1974, *Phys. Rev. A*, 10, 829
- Lim, J., Carilli, C. L., White, S. M., Beasley, A. J., & Marson, R. G. 1998, *Nature*, 392, 575
- Ludwig, H.-G., Caffau, E., Steffen, M., et al. 2009, *Mem. S.A.It.*, 80, 711
- Magic, Z., Collet, R., Asplund, M., et al. 2013, *A&A*, (in preparation)
- Mathisen, R. 1984, in *Inst. Theor. Astroph. Publ. Ser.*, Vol. 1, Photo Cross-Sections for Stellar Atmosphere Calculations – Compilation of References and Data (University of Oslo), 1–63
- Mathur, S., Hekker, S., Trampedach, R., et al. 2011, *ApJ*, 741, 119
- Mathur, S., Metcalfe, T. S., Woitaszek, M., et al. 2012, *ApJ*, 749, 152
- Meyer, C. W., Cannell, D. S., & Ahlers, G. 1992, *Phys. Rev. A*, 45, 8583
- Miesch, M. S., Elliot, J. R., Toomre, J., et al. 2000, *ApJ*, 532, 593
- Mihalas, D. 1978, *Stellar atmospheres*, 2nd edn. (W. H. Freeman and Company)
- Mihalas, D., Däppen, W., & Hummer, D. G. 1988, *ApJ*, 331, 815
- Namba, O., & van Rijsbergen, R. 1977, in *IAU Coll. 38, Lecture Notes in Physics*, Vol. 71, Problems of Stellar Convection, ed. E. A. Spiegel & J. P. Zahn (Berlin: Springer), 119–125
- Nordlund, Å. 1982, *A&A*, 107, 1
- Nordlund, Å., & Dravins, D. 1990, *A&A*, 228, 155
- Nordlund, Å., & Stein, R. F. 1990, *Comput. Phys. Commun.*, 59, 119
- Nordlund, Å., & Stein, R. F. 1991a, in *Stellar Atmospheres: Beyond Classical Models*, ed. L. C. et al. (Dordrecht: Kluwer), 263–279
- Nordlund, Å., & Stein, R. F. 1991b, in *Lecture Notes in Physics*, Vol. 388, Challenges to Theories of the Structure of Moderate-Mass Stars, ed. D. O. Gough & J. Toomre (Berlin: Springer), 141–146
- Nordlund, Å., & Stein, R. F. 1997, in *Solar Convection and Oscillations and their Relationship*, ed. F. P. Pijpers, J. Christensen-Dalsgaard, & C. S. Rosenthal (Dordrecht: Kluwer), 79–103
- Nordlund, Å., Stein, R. F., & Asplund, M. 2009, *Living Rev. Solar Phys.*, Vol. 6, Solar Surface Convection, 2nd edn. (Katlenburg-Lindau, Germany: MPIS), cited 19.05.2009, <http://www.livingreviews.org/lrsp-2009-2>
- Paxton, B., Bildsten, L., Dotter, A., et al. 2011, *ApJS*, 192, 3:1
- Perryman, M. A. C., de Boer, K. S., Gilmore, G., et al. 2001, *A&A*, 369, 339
- Prusti, T. 2012, *Astron. Nach.*, 333, 453
- Radau, R. 1880, *J. Math. Pures et Appl.*, 6, 283
- Rast, M. P. 1995, *ApJ*, 443, 863
- Renka, R. J. 1984, *ACM Trans. on Math. Softw.*, 10, 440
- Robinson, F. J., Demarque, P., Li, L. H., et al. 2003, *MNRAS*, 340, 923
- Rosenthal, C. S., Christensen-Dalsgaard, J., Nordlund, Å., Stein, R. F., & Trampedach, R. 1999, *A&A*, 351, 689
- Schwarzschild, M. 1975, *ApJ*, 195, 137
- Skartlien, R. 2000, *ApJ*, 536, 465
- Spruit, H. C., Nordlund, Å., & Title, A. M. 1990, *ARA&A*, 28, 263
- Stancil, P. C. 1994, *ApJ*, 430, 360
- Stein, R. F., & Nordlund, Å. 1989, *ApJ*, 342, L95
- Stein, R. F., & Nordlund, Å. 1991, in *Lecture Notes in Physics*, Vol. 388, Challenges to Theories of the Structure of Moderate-Mass Stars, ed. D. O. Gough & J. Toomre (Berlin: Springer), 195–212
- . 1998, *ApJ*, 499, 914
- Stein, R. F., & Nordlund, Å. 2003, in *Stellar atmosphere modeling*, ed. I. Hubeny, D. Mihalas, & K. Werner, *ASP Conf. Ser. No. 288*, 519–532
- Trampedach, R. 1997, Master's thesis, Aarhus University, Århus, Denmark
- Trampedach, R. 2002, in *Local and Global Helioseismology: The Present and Future*, ed. H. Sawaya, *SOHO 12/Gong 2002 Workshop* (Noordwijk: ESA), 195–200
- Trampedach, R. 2007, in *Unsolved Problems in Stellar Physics: A Conference in Honor of Douglas Gough*, ed. R. J. Stancilffe, G. Houdek, R. G. Martin, & C. A. Tout, *Conf. Proc. No. 948*, *AIP* (Melville, NY: AIP), 141–148
- Trampedach, R. 2012, in *The Modern Era of Helio- and Asteroseismology*, ed. M. Roth & K. Uytterhoeven, *Astron. Nachr. Conf. Series, ESF* (Berlin: Wiley-VCH), (submitted)
- Trampedach, R., Christensen-Dalsgaard, J., Nordlund, Å., Asplund, M., & Stein, R. F. 2013, *A&A*, (in preparation)
- Trampedach, R., & Stein, R. F. 2011, *ApJ*, 731, 78:1
- Victor, G. A., & Dalgarno, A. 1969, *J. Chem. Phys.*, 50, 2535
- Walker, G., Matthews, J., Kuschnig, R., et al. 2003, *PASP*, 115, 1023
- Wedemeyer, S., Freytag, B., Steffen, M., Ludwig, H.-G., & Holweger, H. 2004, *A&A*, 414, 1121
- Wishart, A. W. 1979, *MNRAS*, 187, 59
- Yan, Y., & Seaton, M. J. 1987, *J. Phys. B*, 20, 6409